

Non-Line-of-Sight 3D Object Reconstruction via mmWave Surface Normal Estimation

Laura Dodds¹, Tara Boroushaki¹, Kaichen Zhou¹, Fadel Adib^{1,2}

{ldodds,tarab,zhouk777,fadel}@mit.edu

¹ Massachusetts Institute of Technology, ² Cartesian Systems

Abstract

This paper presents the design, implementation, and evaluation of mmNorm, a new and highly-accurate method for non-line-of-sight 3D object reconstruction using millimeter wave (mmWave) signals. In contrast to past approaches for millimeter-wave-based imaging that perform backprojection for 3D object reconstruction, mmNorm reconstructs the surface by estimating the object's surface normals. To do this, it introduces a novel algorithm that directly estimates the surface normal vector field from mmWave reflections. By then inverting the normal field, it can reconstruct structural isosurfaces, then solve for the exact surface through a novel mmWave optimization framework.

We built an end-to-end prototype of mmNorm using a TI IWR1443 Boost mmWave radar and a UR5e Robotic Arm, and evaluated it in over 110 real-world experiments across more than 60 different everyday objects. In a head-to-head comparison with state-of-the-art baselines, mmNorm achieves 96% reconstruction accuracy (3D F-score) compared to 78% for the best-performing baseline. These results show that mmNorm is capable of high-accuracy mmWave object reconstruction. The codebase and a video demonstration are available here: <https://github.com/signalkinetics/mmNorm>

CCS Concepts

• Computer systems organization → Sensor networks; • Networks → Sensor networks.

Keywords

Non-Line-of-Sight 3D Reconstruction, Millimeter-Wave Imaging, Millimeter-Wave Sensing, Surface Normal Estimation, Robotic Manipulation

ACM Reference Format:

Laura Dodds, Tara Boroushaki, Kaichen Zhou, Fadel Adib. 2025. Non-Line-of-Sight 3D Object Reconstruction via mmWave Surface Normal Estimation . In *The 23rd Annual International Conference on Mobile Systems, Applications and Services (MobiSys '25)*, June 23–27, 2025, Anaheim, CA, USA. ACM, New York, NY, USA, 14 pages. <https://doi.org/10.1145/3711875.3729138>

1 Introduction

The past few years have witnessed growing interest in millimeter wave (mmWave) based reconstruction in the mobile community [12, 19, 24, 77]. Unlike classical vision-based imaging systems, which are limited to line-of-sight, these mmWave-based systems can operate in non-line-of-sight (NLOS) conditions, enabling them to sense objects in closed boxes and beneath occlusions. This is because



This work is licensed under a Creative Commons Attribution-NonCommercial- ShareAlike 4.0 International License.

MobiSys '25, Anaheim, CA, USA

© 2025 Copyright held by the owner/author(s).

ACM ISBN 979-8-4007-1453-5/2025/06

<https://doi.org/10.1145/3711875.3729138>

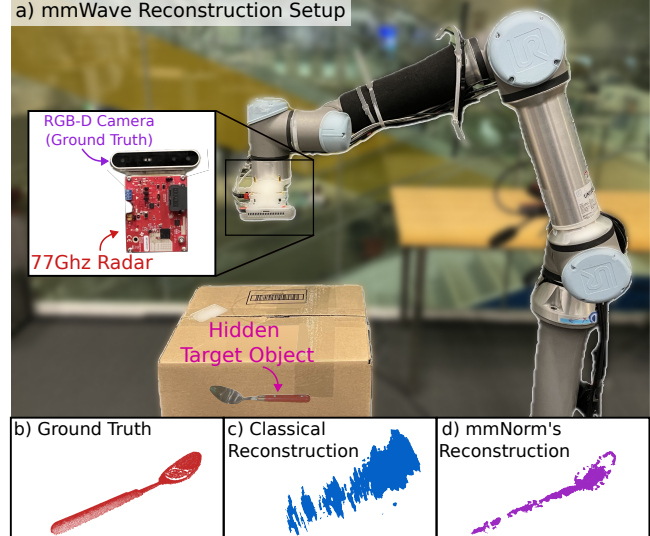


Figure 1: mmNorm. a) We build a real-world prototype with a 77 GHz radar, robotic arm, & RGB-D camera for ground-truth. b) The ground-truth surface of a spoon. c) Classical mmWave reconstruction produce poor 3D reconstruction. d) mmNorm achieves high accuracy reconstructions.

mmWave signals can traverse through many everyday occlusions (e.g., cardboard, fabric, etc) [6, 41, 47], and reflect off objects behind these occlusions, allowing them to produce images of the occluded objects. This capability, combined with the recent emergence of low-cost commercial mmWave radars, has the potential to enable many promising applications. For example, pick-and-place robots can leverage non-line-of-sight reconstructions to find and manipulate hidden objects, such as those beneath clutter or within a closed box. Similarly, Augmented Reality (AR) devices could leverage them to perceive occluded objects and display them to the user, truly augmenting our human perception. Smart home devices can use them for NLOS gesture recognition, to enable non-verbal commands even when users are hidden from view.

However, enabling these applications requires accurate 3D object-level reconstructions. For example, robots rely on precise 3D reconstructions to reason about complex interactions with the environment, and execute successful manipulation tasks (e.g., grasping, pushing, etc). Additionally, more representative object reconstructions would significantly improve AR user experience. Furthermore, smart home devices would require precise reconstructions to identify small differences between gestures and execute the corresponding commands.

Unfortunately, existing approaches for mmWave-based 3D object reconstruction cannot deliver on these applications due to their low accuracy. To see why, it is helpful to first understand a typical mmWave reconstruction output in a real-world setting, such as the one shown in Fig. 1. Here, we attached a commercial mmWave

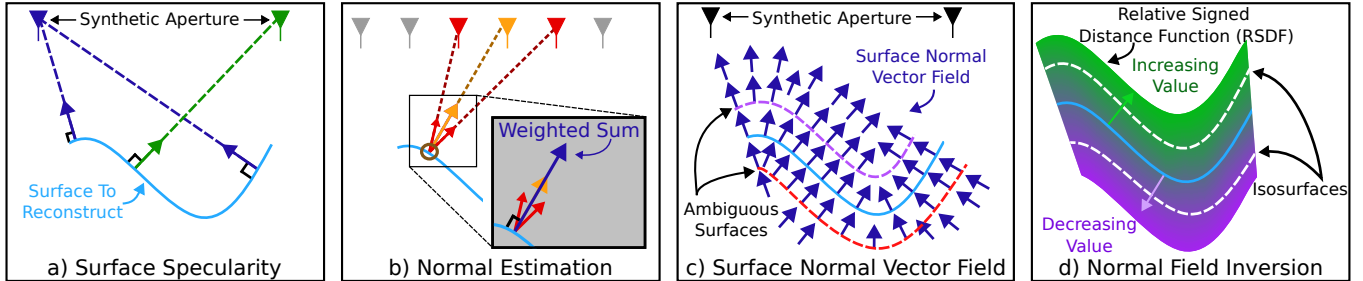


Figure 2: mmNorm’s Design. a) Only some points on the surface will reflect signals back to the radar, due to specularity. b) mmNorm estimates normals through a coherent filter. c) mmNorm produces a normal vector field. d) mmNorm represents all valid reconstructions through a RSDF.

radar to a robotic arm,¹ as shown in Fig. 1a, and used an RGB-D camera to provide the ground truth.² Fig. 1b shows the ground-truth point cloud in red, and Fig. 1c shows a standard mmWave point cloud reconstruction in blue [19]. Here, the classical mmWave reconstruction approach does not accurately represent the surface geometry. For example, the classical reconstruction contains points spread across a wide volume in space. In fact, the reconstruction covers a volume almost twice the size of the original object. This poor level of reconstruction would, for example, make it difficult for a robot to plan successful grasps for this object, since it is difficult to identify the location of the handle.

The reason why existing approaches are limited is inherent to how they perform 3D reconstruction. Specifically, the vast majority of existing approaches start by leveraging a raytracing-based imaging algorithm (such as backprojection [79] or the range-migration algorithm [25, 68]) to generate a 3D mmWave image. Then, this image is directly used to generate an occupancy distribution. For example, to create object point clouds, it is common to select all voxels in the 3D mmWave image above a certain power threshold [7, 19, 24], as we demonstrated in the example above.

Unfortunately, this approach is limited by the available bandwidth of the mmWave radar. Since commercial mmWave radars have a bandwidth of at most about 4GHz³, their depth resolution is limited to ~4cm, which leads to a corresponding distortion in occupancy-distribution based point clouds. This is why, in the above example, the reconstruction is smeared in the depth (vertical) dimension. While this resolution is sufficient for reconstructing large objects, such as buildings or vehicles [7, 24, 57], it is not sufficient for applications that require object-level 3D reconstruction. For example, a pick-and-place robot requires sub-cm reconstruction quality to reliably grasp an object, such as a tool, bottle, or utensil[64].

In this paper, we depart from this classical approach, and propose mmNorm, a fundamentally new method for mmWave 3D object reconstruction. Let us first see the benefit of our method through a real-world result in Fig. 1d. Here, our reconstruction (purple) closely matches the ground-truth and significantly outperforms the classical method.

Our key idea behind mmNorm’s design is that, instead of estimating occupancy distribution from ray tracing, we directly estimate

the object’s curvature, then use this to generate a high-accuracy 3D reconstruction. We explain our high-level approach through Fig. 2. First, to estimate an object’s curvature, we rely on the fact that most objects exhibit primarily specular (i.e., mirror-like) reflections at mmWave frequencies [43]. This creates a relationship between the radar’s received reflections and the object’s surface normals (which define an object’s curvature). For example, in Fig. 2a, when measuring the response from the surface (shown in light-blue), the antenna location on the left (shown in the dark-blue) will primarily receive reflections from the two points on the surface where the normal (shown by dark blue arrows) points directly towards the antenna. Other points on the surface will mostly reflect signals away from that antenna’s location. In another example, the antenna location shown in green will receive responses from a different point on the surface (shown by the green arrow).

Using this core insight, we design mmNorm to estimate surface normals and use these to directly estimate the object’s curvature. At the heart of its method is the following fundamental observation: each point on the object’s surface has a surface normal that is directed toward the antenna position receiving that point’s strongest reflection. mmNorm’s goal is to solve the inverse problem to this observation. To do so, its method introduces the following three techniques:

1. *mmWave Surface Normal Estimation.* First, mmNorm aims to estimate the surface normals of the object through a coherent filter using mmWave reflections. Let us explain this method using the illustration shown in Fig. 2b. The figure shows an object’s surface in light blue, and the brown circle highlights the point for which we will estimate the surface normal vector. We start by constructing “candidate” surface normals from this point towards each radar location. Then, we allow different radar locations to “vote” on the direction of the normal based on the reflections received at that location. For example, the orange radar location receives a strong reflection from this point, so it will cast a strong vote shown by the orange arrow. In contrast, the red radar locations receive weaker reflections and therefore will cast weaker votes. Finally, we geometrically combine these votes to produce a final normal estimate, as shown by the dark blue arrow. Since this method is applied to every point in 3D space, not just points on the surface (as their locations are unknown *a priori*), it results in a normal vector field like that shown by the dark blue arrows in Fig. 2c. We describe this method, including how we design a coherent filter to produce each radar’s “vote”, in more details in §2.

2. *mmWave Normal Field Inversion.* Next, mmNorm aims to invert the field to produce the surface geometry. However, each vector field

¹The robotic arm moves the mmWave radar to construct a synthetic aperture radar, similar to prior work [6, 19].

²While the mmWave image is collected in NLOS, to capture the ground truth, we remove the occlusion to capture an RGB-D image in line-of-sight.

³The bandwidth is typically limited by government regulations. While some work has investigated reconstruction with larger bandwidths, these systems are restricted to non-commercial or government use [16].

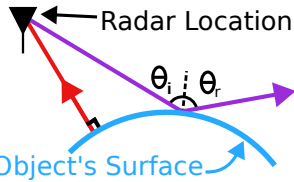


Figure 3: Specular reflection. Only some points reflect signals back to radar.

defines multiple possible surfaces. For example, Fig. 2c shows two example surfaces in red and purple which are valid reconstructions defined by the vector field, but are far from the ground-truth surface shown in light blue. Thus, it is infeasible to directly recover a single surface from the vector field. To address this, our next step is *mmWave Normal Field Inversion*. Here, we adapt a technique from computer vision called Signed Distance Function. Specifically, we design a *Relative* Signed Distance Function (RSDF), which enables us to model all possible reconstructions as isosurfaces⁴ of a single 3D implicit function. We show an example of this function with the color gradient in Fig. 2d. In §3, we describe how we adapt this technique to our problem domain to invert the mmWave vector normal field by accounting for the RF and geometric characteristics of the mmWave field.

3. mmWave Structural Isosurface Optimization. The final step of mmNorm’s design aims to select the optimal isosurface. This technique overcomes the aforementioned surface ambiguity by evaluating how well different candidate isosurfaces correspond to our received signals. To do this, for a given isosurface, it simulates the signal that would be reflected from that surface to each radar location. Then, it formulates a cost function as the difference between these simulated signals and actual received signals. By optimizing across cost, it can identify optimal isosurfaces, as we detail in §4.

We built an end-to-end prototype of mmNorm, consisting of a TI IWR1443Boost radar attached to a UR5e robot arm. The robot moves the radar to produce a 2D synthetic aperture above the target object. We evaluate the 3D surface reconstruction across over 60 objects in the MITO dataset [18], a mmWave dataset of common everyday objects for robotic manipulation. We include results in both line-of-sight and non-line-of-sight. Our empirical evaluation demonstrates that:

- mmNorm achieves 96% reconstruction accuracy (3D F-score), compared to 78% for the best-performing baseline.
- By zooming in on individual points, our evaluation shows that in the best-performing baseline, only 44% of the points have less than 5% reconstruction error (displacement error relative to object’s size), in contrast to 85% for mmNorm.

Contributions: This paper presents mmNorm, a first-of-its-kind method for mmWave-based 3D object reconstruction, which operates using surface normal estimation. It introduces multiple innovations, including *mmWave Surface Normal Estimation*, *mmWave Normal Field Inversion*, and *mmWave Structural Isosurface Optimization*. Finally, the paper also contributes an end-to-end prototype and real-world evaluation, which demonstrates its accuracy and robustness.

In reflecting on these results, one might wonder how mmNorm achieves such high-accuracy reconstruction without additional

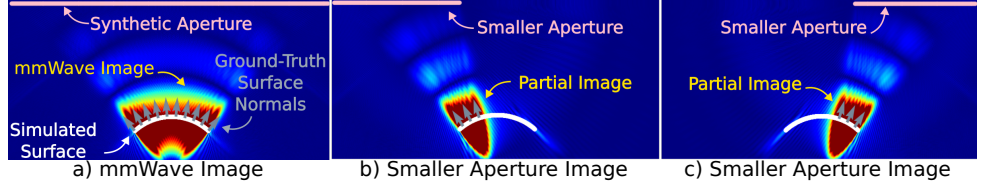


Figure 4: The Surface Normal to mmWave Image Relationship. The mmWave image will only contain the portion of the surface with normals pointing within the aperture.

bandwidth. In backprojection-based reconstruction, there is a direct relationship between the available bandwidth and the resulting resolution. In contrast, mmNorm operates in a different subspace. The mathematical derivation of this subspace, and the theoretical limitations of mmNorm is an interesting avenue for future work.

2 mmWave Surface Normal Estimation

The first step of mmNorm’s reconstruction pipeline is to directly estimate an object’s surface normal vector field from mmWave reflections. In this section, we first describe the underlying relationship between the object’s surface normal, the radar location, and the resulting mmWave image. Then, we describe how we leverage this relationship when designing our mmWave surface normal field estimation algorithm.

2.1 The Normal to Image Relationship

To understand the impact of an object’s surface normals on its mmWave image, it is helpful to understand how the mmWave image is obtained in the first place. Typical mmWave imaging systems leverage the concept of synthetic aperture radar [38, 44]. In these systems, a radar is moved through space to collect measurements from different locations, which together form a “synthetic aperture”. At each location in the synthetic aperture, a radar transmits a signal, which reflects off the object and is received back at the radar.

However, the radar will not receive reflections from all points on the object’s surface. This is because, at mmWave frequencies, most objects exhibit primarily specular (i.e., mirror-like) reflections [43], where the angle of incidence is equal to the angle of reflection.⁵ This phenomenon can be seen through Fig. 3, where we demonstrate it in 2D for simplicity. Here, we show one radar location within the synthetic aperture in black. First, we consider a signal transmitted along the purple line. In this case, the signal will reflect off the light-blue object and away from the radar (due to specularity), preventing the radar from ever receiving this reflection. Next, we consider a signal transmitted along the red line. In this case, the signal is reflected back to the radar, allowing the radar to properly receive the reflection. This is because this portion of the surface has a normal, shown by the red arrow, which is directed towards the radar. Thus, the radar will only receive reflections from the portions of the surface where the normal points directly towards the radar.

This phenomenon creates a relationship between the radar locations, the object’s surface normal, and the resulting mmWave image. We demonstrate this through an example in Fig. 4. Here, we show the cross-section view of a simulated mmWave image, where the

⁵A surface is considered electromagnetically smooth if the surface height variations are less than $\frac{\lambda}{8\cos(\theta_i)}$, where θ_i is the incident angle [53]. For a 77 GHz system, surfaces exhibit diffuse scattering reflections when surface height variations are $>0.49\text{mm}$, which is very rough to human touch.

⁴An isosurface is a surface where the value of a 3D function is constant.

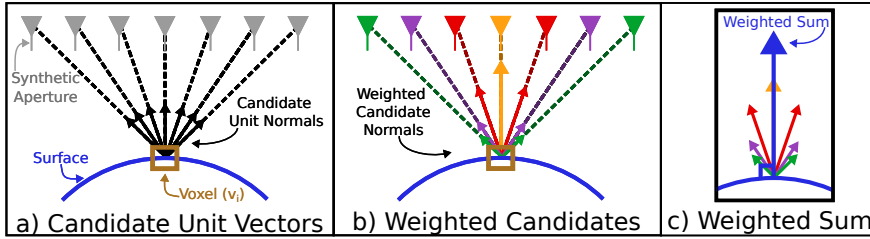


Figure 5: mmWave Normal Estimation. mmNorm estimates normal vectors by a) constructing candidate vectors, b) weighting them via a coherent filter, and c) combining them through a weighted sum

simulated aperture is shown by the pink line, the simulated surface is shown by the white line, and the surface's ground truth normal vectors are shown by the gray arrows. We simulated the received reflections at each radar location using a standard free-space path loss simulation [18, 72], and produced a mmWave image using the standard near-field backprojection algorithm [79]. The heatmap shows the magnitude of the resulting mmWave image, where red and blue represents areas of high and low reflection power, respectively. In the first example in Fig. 4a, the full surface is contained within the red region of the image. This is because all of the surface's normal vectors point within the aperture, so reflections from every portion of the surface can be received from at least one radar location. Next, we show two more examples in Fig. 4b/c, where we image the same surface with a smaller portion of the aperture. Here, only a small portion of the surface is within the red region. This is because these sub-apertures only receive reflections from the portions of the surface where the normal vectors are pointing within the sub-aperture, and all other portions of the surface reflect signals away (due to specularity).

Based on these results, we can now understand the following two key points about the relationship between the mmWave image and the object's surface normals:

- If we incorporate measurements only from a small sub-aperture in the imaging, we will only see part of the surface – i.e., other parts entirely disappear as we see in Fig. 4b/c.
- The portion of the surface that can be seen in the mmWave image depends on the normals – i.e., we will only see the portion with normals pointing towards the sub-aperture.

These observations reveal the relationship between the normal vector, radar location, and mmWave image value.

Note, however, that the mmWave image alone is not enough to reconstruct the surface. This is because while the surface (white) lies within the red region in the mmWave image of Fig. 4a, the red region covers a much larger area than the surface itself (due to limited bandwidth). This necessitates a more sophisticated approach for surface normal estimation.

2.2 mmWave Normal Field Estimation

Next, we describe how we can leverage the above relationship to design a surface normal estimation algorithm.

To start, we consider a single voxel in 3D space. If we draw a straight line between the voxel and each radar location, we would trace out different candidate normal vectors. Then, if we can identify which radar locations contributed the most to this voxel's mmWave image value,⁶ we can combine their candidate vectors to form our final estimate of the surface normal at that point. The

⁶Here, the mmWave image refers to one similar to that of Fig. 4.

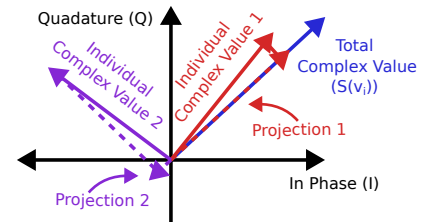


Figure 6: mmWave Coherent Filter. Our coherent filter employs projection magnitudes.

question becomes: how do we identify the radar locations that contribute most?

To answer this question, we break each voxel's mmWave image value down into the components that result from each individual radar location within the aperture. We then allow each radar location to "vote" on the direction of the surface normal based on how strongly it contributes to the voxel's mmWave image. By geometrically combining the votes, we can estimate the surface normal.

We explain how our method estimates the normal at a given voxel v_i , using Fig. 5 as an example. The figure depicts an example scenario, where an object surface is shown in blue, and the given voxel is outlined in brown. We describe our method through the following three steps:

- (1) First, we construct a set of candidate normal vectors. For example, Fig. 5a shows the candidate vectors as black arrows, where each candidate is a unit vector pointing from the voxel towards one radar location (shown in gray) within the synthetic aperture. Formally:

$$\mathbf{u}_{i,j} = \frac{\mathbf{p}_j - \mathbf{v}_i}{\|\mathbf{p}_j - \mathbf{v}_i\|} \quad (1)$$

where $\mathbf{u}_{i,j}$ is the candidate unit normal vector pointing from voxel v_i to the j^{th} radar location p_j .

- (2) Next, we allow each radar location to "vote" on the correct surface normal. We do so by using the received signal from each radar location to assign a weight to its associated candidate vector. This is shown in Fig. 5b, where the colored arrows represent the weighted candidate vectors. Vectors in the direction of the surface normal will have a large weighting, such as the orange vector. We describe our method for calculating this weighting function in §2.2.1. Formally, our weighted candidates are:

$$\mathbf{r}_{i,j} = w_{i,j} \mathbf{u}_{i,j} \quad (2)$$

where $\mathbf{r}_{i,j}$ is the j^{th} weighted candidate vector for voxel v_i . $w_{i,j}$ is the weighting value for the j^{th} radar location.

- (3) Finally, we compute the final surface normal estimate as the weighted sum of all candidate vectors, as shown by the blue arrow in Fig. 5c. Formally:

$$\hat{\mathbf{n}}_i = \frac{1}{\|\sum_{j=1}^A \mathbf{r}_{i,j}\|} \sum_{j=1}^A \mathbf{r}_{i,j} \quad (3)$$

where $\hat{\mathbf{n}}_i$ is the (normalized) surface normal vector estimate, and A is the number of radar locations.

By applying the above process for each voxel in 3D space, we estimate the full surface normal vector field of the object.

2.2.1 mmWave Candidate Weighting Function. Next, we describe how we compute the weighting values for different candidate vectors of a given voxel (i.e., step 2 above). At a high level, our weight-

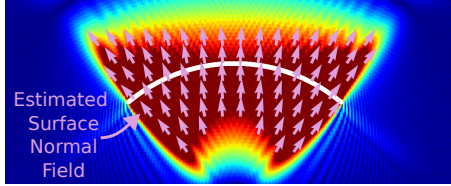


Figure 7: Estimated Normal Field. mmNorm’s estimated surface normal field (pink arrows) for a simulated scene.

ing values depend on a coherent filter which we design to identify how much each radar location contributes to the final mmWave image value at this voxel.

To understand our filter design, it is helpful to first understand how the mmWave image is created. Consider a mmWave image which is constructed using the standard near-field matched-filter method [79]. In this case, to compute the image value at a given voxel, the algorithm first computes individual values from each radar location. It does so by correlating each received signal with the appropriate round-trip distance to the voxel. Formally, since mmWave radars typically leverage frequency-modulated continuous waves (FMCW), we apply a wide-band correlation as:

$$I_j(v_i) = \sum_{t=1}^T h_j(t) e^{j2\pi(2||p_j - v_i||)/\lambda_t} \quad (4)$$

where $I_j(v_i)$ is the complex value of v_i for the j^{th} individual radar location. λ_t is the wavelength of the t^{th} sample (out of T) in the FMCW chirp, $h_j(t)$ is the t^{th} sample of the time-domain baseband received signal from the j^{th} radar location.

Then, the final complex voxel value, $S(v_i)$, is computed as the sum across all the values from individual radar locations:

$$S(v_i) = \sum_{j=1}^A I_j(v_i) \quad (5)$$

Now, the goal of our filter is to determine how much each individual voxel value, $I_j(v_i)$, contributed to the final complex sum, $S(v_i)$. To do so, we project the individual voxel values onto the computed sum, $S(v_i)$. We show two examples in red and purple in Fig. 6, which plots the complex values as vectors on the IQ plane. It is important to note that these vectors represent complex values, and not the direction of candidate surface normal vectors. The final mmWave voxel value ($S(v_i)$) is shown as the blue vector. First, we consider an antenna which is in the direction of the surface normal. Since it received a strong reflection from this voxel, its complex value (red) will contribute strongly to the sum, and thus will point in a similar direction as the sum. Therefore, its projection onto the sum (the dotted red arrow) will have a large magnitude. Next, we consider an antenna not in the direction of the normal. It will not receive a strong reflection from this voxel, and thus its value will not be related to the sum. Here, its complex value (purple) will point in a different direction, and its projection magnitude will be low.

Using this intuition, we define our weighting function for the candidate unit vectors to be the magnitude of the projection of individual voxel values onto the final sum. Formally:

$$w_{i,j} = \frac{\Re\{I_j(v_i)\}\Re\{S(v_i)\} + \Im\{I_j(v_i)\}\Im\{S(v_i)\}}{||S(v_i)||} \quad (6)$$

where $\Re\{\cdot\}$ and $\Im\{\cdot\}$ are the real and imaginary components of a

complex number, respectively.

We can then use this weighting function to compute the final normal estimate, as described previously, using Eqs. 1-3.

Finally, we repeat this process for each voxel to estimate the full surface normal vector field. Fig. 7 shows an example of mmNorm’s estimated normal field (as pink arrows) for the simulated scene we presented earlier (in Fig. 4a).⁷ Here, the direction of the estimated vectors closely match the object’s curvature, showing the success of our proposed approach.

A few additional points are worth noting:

Generalizing to Non-Specular Reflections: While our explanation thus far has relied on the fact that surfaces exhibit primarily specular reflections, our method still applies to cases with some level of diffuse scattering. For mmWave frequencies, diffuse reflections from many surfaces can be modeled with the directive model [4, 50], where the reflection power is symmetric around the specular angle, but spread across a range of angles. This model applies to many common materials spanning concrete, drywall, and marble [4, 50]. When the reflected power is symmetric around the specular angle, two weighted candidate vectors on opposite sides of the surface normal will still sum to the direction of the normal. For example, in Fig. 5b, the two red vectors sum to the direction of the object’s normal. This allows directive diffuse reflections to further reinforce our normal estimate.

Behavior of Weighting Function: For radar locations which are not in the direction of the surface normal (e.g., the green & purple radar locations in Fig. 5b), the projection magnitudes are not always low. At first glance, this might appear to be an issue, since the large projection magnitudes would result in strongly weighted (and incorrect) candidate vectors, which one would expect to distort the final normal estimate. However, it can be shown that the projection magnitudes for radar locations far from the normal direction oscillate, producing both positive and negative weights. This causes these weighted candidate vectors to point in opposite directions. Thus, they cancel when summed together, preventing these radar locations from influencing the final normal estimate.

Non-Uniform Object Properties: At first glance, it may appear that mmNorm requires the object to exhibit uniform properties (e.g., material, reflection power, etc) across the object surface. However, this is not the case. It is important to note that mmNorm is not solving the problem, “for a given radar location, which point on the surface produces the strongest reflection?”, but the inverse, “For a given point on the surface, which radar location receives the strongest reflection?” For example, in Fig. 5, we compare the response at a single point on the surface (the brown voxel) across all radar locations. Thus, relative changes across the surface of the object have minimal impact. We demonstrate mmNorm’s ability to reconstruct objects with variable properties (e.g., multiple materials) in §6.

3 mmWave Normal Field Inversion

Now that we have described mmNorm’s approach to estimating a surface normal field we can move on to inverting this field to recover the surface.

⁷We only show the portion of the estimated vector field which lies within the high-power (red) region of the mmWave image, since other locations suffer poor signal-to-noise ratio and thus poor normal estimation accuracy.

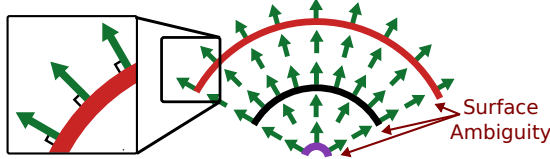


Figure 8: Surface Ambiguity. The vector field (green arrows) for a ground-truth surface (black) can represent multiple surfaces (red & purple).

3.1 The Surface Ambiguity Problem

Typically, one can convert an object’s surface normals to the object shape by finding the surface that is perpendicular to every normal vector. However, when given a normal vector field, there are multiple such surfaces. We show this through an example in Fig. 8. Here, we show a ground-truth surface in black, and its normal vector field as green arrows. Based on this visualization, it becomes clear that we can construct multiple possible surfaces for this vector field, such as the two examples in red and purple. Each of these surfaces is perpendicular to the normal vectors within this field, and is therefore a valid possible surface.

3.2 Relative Signed Distance Function

To address this, our idea is to generate an implicit function capturing all possible surfaces, and in §4 we will describe how we optimize across this function to find the final surface.

To capture the object’s shape, we design an implicit function similar to a signed distance function (SDF) from the computer graphics and vision community [66]. An SDF is a 3D function which defines, at each point in space, the distance from this point to the nearest point on the object’s surface. Typically, an SDF is zero on the object’s surface, positive outside the surface, and negative inside the surface.

In our case, since we cannot identify the object’s surface directly, we cannot find the exact SDF. Instead, we define a new implicit function called a Relative Signed Distance Function (RSDF), which is an SDF that is offset by an unknown constant. For example, Fig. 2d shows an example of a 2D cross-section of an RSDF function as a color gradient, where brighter green represents increasing values, and brighter purple represents decreasing (negative) values.

Unlike a standard SDF, where the object’s surface is defined by the zero level-set, the RSDF cannot be used to directly identify the object’s surface. Instead, we will use the RSDF to define all possible ambiguous surfaces through its different isosurfaces. An isosurface is a 3D surface where a function is the same value across the whole surface [66]. For example, Fig. 2d shows two example isosurface cross-sections as white lines. For each of these lines, the color (and therefore RSDF value) is constant across the whole line. Due to the construction of the RSDF, this means that each isosurface is one valid reconstruction for the given normal vector field.

To generate our RSDF, we rely on the fact that a normal vector field is the gradient of the SDF [32]. Thus, we can generate an RSDF via a surface integral over our vector field. This integral will be offset from the standard SDF, since we do not know where within the integral the zero level-set is.

Next, we formalize how to compute this surface integral. We will approximate the integral as a discrete summation, since our vector field is defined along discrete voxels. To start we choose a voxel, v_0 , to act as a starting point. We assign the RSDF at this voxel to 0, and will compute remaining RSDF values relative to this voxel.

Formally, the RSDF f^R at v_0 is:

$$f^R(v_0) = 0 \quad (7)$$

Next, to compute the RSDF value at another voxel v_i , we first find a path of voxels from v_0 to v_i . Then, we apply a discrete summation along this path to find the RSDF at v_i .

$$f^R(v_i) = \sum_{k \in P} (\hat{n}_k \cdot d_k) + f^R(v_0) \quad (8)$$

where P is a path of voxels connecting v_0 to v_i , and d_k is the vector along the path P , pointing from voxel v_{k-1} to v_k .⁸

Now, the absolute SDF, f , is a constant offset, C , from f^R :

$$f(v_i) = f^R(v_i) - C \quad (9)$$

Now, all possible surfaces are captured as different isosurfaces within $f^R(v_i)$ (or $f(v_i)$). Furthermore, the problem of finding the correct surface can be reduced to finding the proper offset constant C , and then taking the zero level-set of the final SDF as the object surface estimate.

3.2.1 Dealing with Complex Surfaces. So far, our discussion has focused on scenarios where the object exposes a single surface curvature. For example, the top side of a box facing the mmWave radar consists of one flat surface, while a cylinder exposes one continuous, curved surface. However, many objects contain more complex curvatures. For example, a spatula contains multiple surface components: one rounded portion for the handle and one flat portion for the flipper.

This becomes a problem if we cannot capture the full normal vector field connecting these different surface components. For example, recall from §2.1 that a synthetic aperture is only capable of capturing reflections from portions of the surface whose normal vectors point within the aperture. Therefore, if there is a portion of the spatula’s handle, for example, which has normals pointing outside the aperture, there will be gaps within our estimated normal vector field. This creates a problem when recovering the full surface, since the relative change in the surface within that missing component will not be recovered. It also creates a discontinuity in the normal vector field which is difficult to invert.

To address this challenge, we leverage the original mmWave image to identify different captured portions of the object and compute the RSDF for each independently. Here, it is important to recall that the mmWave image, such as the one shown in Fig. 4, does not have enough resolution for surface reconstruction, but often has more than enough information to localize different portions of the objects. We realize the above approach by identifying contiguous areas of the surface as areas of high reflection power in the image.

We explain our method through an example in Fig. 9, which contains results from a real-world, non-line-of-sight experiment for different stages of our method. Here, we consider 2D cross section of a mug on its side with two separate surface components: one large, curved surface for the cup, and one small surface for the handle. Fig. 9a shows the ground-truth surface as a pink line, and the initial mmWave image as a heatmap. As described previously, the mmWave image does not capture the full object. This is shown in the region circled in white, which appears dark blue in the image. Our approach to overcome this is composed of three steps:

⁸We compute this with dynamic programming.

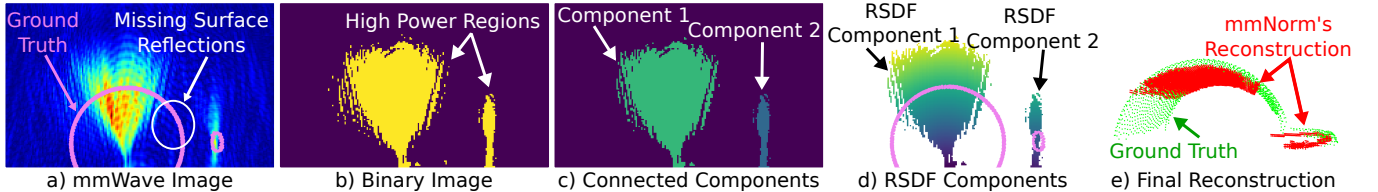


Figure 9: Dealing with Complex Objects. For this example of mug, a) the mmWave image will not capture the entire surface. b) We separate the image into high-power regions and c) find the connected components. d) We construct separate RSDFs for each component. e) mmNorm's final reconstruction.

- (1) First, we convert the mmWave image into a binary image. We assign all voxels above a threshold to 1, and all voxels below the threshold to 0. This can be seen in Fig. 9b, where the purple/yellow regions indicate 0/1. Here, there are two main yellow regions corresponding to the two different surface portions of the object. Formally,

$$m(v_i) = \begin{cases} 1 & \text{if } |S(v_i)| > \tau \\ 0 & \text{else} \end{cases} \quad (10)$$

where $m(v_i)$ is the binary image, and τ is the threshold.⁹

- (2) Next, we find connected components within the binary image. This can be seen in Fig. 9c, where the blue and teal regions indicate two different components, which each correspond to one portion of the object's surface. To find these components, we can leverage a standard breadth-first-search (BFS) [33].
- (3) Finally, we compute a separate RSDF across each connected component. The output from this step can be seen in Fig. 9d, where the color gradients represent the RSDF components. Lighter colors indicate larger values and darker colors indicate smaller RSDF values.

When we apply the above approach, we will be left with multiple different unknown constants, one for each RSDF component. Then, identifying the proper isosurfaces can be reduced to the problem of finding the vector of constants $C = \{C_1, \dots, C_n, \dots, C_N\}$, and selecting the zero-level set of each SDF component to estimate each object surface component.

4 Structural Isosurface Optimization

To overcome the surface ambiguity problem, we are inspired by work in the computer vision and graphics community on imaging and rendering [32, 66], where the goal is to derive a 3D scene from a 2D image. In these systems, rather than attempting to directly solve the inverse problem (e.g., directly estimating the 3D scene), they instead optimize the scene through different forward models. For example, they construct a 3D scene, simulate its 2D image, and compare it to the target image. Then, they can iteratively update the scene parameters until it properly matches the target image.

We adapt this technique to solve the mmWave isosurface ambiguity problem. Specifically, we construct different isosurfaces from each of our RSDF components. Then, we simulate the radar signal which would be reflected from each of the candidate isosurfaces, and compare it to the actual received signals. Then, we select the optimal isosurfaces as the ones whose simulated reflections best match the real-world received reflections. Our approach follows three key steps:

- (1) To start, we simulate the received reflections from a given set of isosurfaces (e.g., one isosurface per RSDF component). We do so

⁹In our implementation, we select τ with the Li thresholding algorithm [39].

by first using standard ray-tracing to find reflection points along the isosurface in each RSDF component [32]. Then, we apply a standard free-space path loss simulation [72] to compute the total received signal at a given radar location. Formally:

$$\hat{h}_j(t, C) = \sum_{n=1}^N \sum_{r \in R_n(C_n)} \frac{1}{d_r(C_n)} e^{-j2\pi d_r(C_n)/\lambda_t} \quad (11)$$

where $\hat{h}_j(t, C)$ is the t^{th} sample of the estimated time-domain received signal from the j^{th} radar location for the isosurfaces defined by the constants C . $R_n(C_n)$ is the set of rays from the ray tracing which intersect with the n^{th} RSDF isosurface. $d_r(C_n)$ is the round-trip distance along ray r . N is the number of RSDF components.

- (2) Next, we aim to evaluate how well these simulated signals match the real-world received signals. To do so, we formulate a cost function, $L(C)$, which takes the difference between the simulated and actual signals:¹⁰

$$L(C) = \sum_{j=1}^A || |FFT(\hat{h}_j(t, C))| - |FFT(h_j(t))| || \quad (12)$$

- (3) Finally, we choose the isosurface with minimum cost:

$$\hat{C} = \arg \min_C L(C) \quad (13)$$

where \hat{C} is the constant defining our estimated isosurface. We show an example output of our optimization method for the real-world example from Fig. 9. Fig. 9e shows the final 3D surface reconstruction determined through Eq. 13 (red), and the 3D ground-truth (green) of a mug on its side. This example shows how our optimization is able to select isosurfaces for each of the 2 RSDF components to produce a reconstruction which closely matches the ground truth.

One may wonder how this approach is able to successfully select isosurfaces without simulating real-world factors such as noise, surface reflectivity, etc. The reason why is similar to why SAR or antenna array systems work well using the same model without incorporating such factors.

5 Implementation & Evaluation

Physical Setup: The physical setup, as shown in Fig. 1, includes a UR5e robotic arm [63] with a wrist-mounted TI mmWave radar (IWR1443Boost [3] and DCA1000EVM [2]), and a wrist-mounted Intel Realsense depth camera (D415 [30]). The radar is connected to a computer running Windows 10 pro, which captures the data for processing. The robotic arm moves the radars over a 2D grid to create a synthetic aperture above the object. The robot scans at ~ 0.1 m/s. We note that this scanning speed is primarily limited by the time synchronization between the radar and the robot, and can

¹⁰We choose to use the FFT, since there is a direct relationship between the FFT of an FMCW signal and the distance to the isosurface [31]

be improved in future, integrated systems. We move the radars in an $60\text{ cm} \times 45\text{ cm}$ grid (which is large enough to ensure that objects are contained entirely within the aperture), with the target object placed roughly in the center. Our aperture forms a dense grid with $\sim \lambda/4$ spacing between the measurements to prevent aliasing. Our radar collects 512 samples from 77.5GHz-80.5GHz. It has a 6 dB antenna field of view of 100° (horizontal) and 40° (elevation).¹¹

Software: To produce mmWave images, we used a standard near-field backprojection implementation [79] in CUDA. We implemented the processing described in §2- §4 in Python/C++/CUDA on machines running Ubuntu 22.04 with Intel(R) Xeon(R) CPUs and NVIDIA GeForce GTX 1080 GPUs. We compute each image with a voxel size of $1\text{ mm} \times 1\text{ mm} \times 1\text{ mm}$. We evaluate the isosurface optimization (Eq. 13) across isosurfaces sampled every $\lambda/2 \approx 1.9\text{ mm}$.

Computational Complexity: The computational complexity of mmNorm’s normal estimation algorithm (§2) is $O(V \times A)$, where V is the number of voxels and A is the number of antennas. This is similar to the standard backprojection algorithm [17], and is similarly parallelizable. Our RSDF computation (§3) is implemented using a breadth-first search, and thus has a runtime of $O(V)$. Finally, mmNorm’s isosurface optimization (§4) is computed with a complexity of $O(C \times I \times A \times R \times T)$, where R is the number of rays used in raytracing, and I is the number of candidate isosurfaces for each RSDF component. The number of RSDF components, and number of candidate isosurfaces per RSDF can be approximated as scalars (typically <4 and <60, respectively). Thus, the complexity of the optimization is dominated by $O(A \times R \times T)$. This isosurface optimization step is also highly parallelizable.¹²

Evaluation Environment: We evaluated mmNorm in a multipath-rich indoor office setting, with tables, chairs, desks, etc. In our experiments, there were people walking in the background, and standard wireless interference (e.g., WiFi, Bluetooth, etc). For each object, we ran experiments in line-of-sight and non-line-of-sight (fully occluded by a layer of cardboard). The object is placed on a surface $\sim 40\text{cm}$ below the aperture. To allow our evaluation to focus only on target object reconstruction, we minimize background reflections by placing objects on styrofoam [1].

Object Selection: Our evaluation covered 61 different everyday objects from the MITO dataset [18], a mmWave dataset of everyday objects for robotic manipulation. These objects span a wide diversity, including complex objects with multiple surface components (e.g., mug, spatula), composite materials (e.g., power drill, utensils), sharp edges (e.g., knife, scissors), varied curvatures (e.g., flat box vs marble), etc. Furthermore, our objects include a wide variety of material types, including wood, metal, cardboard, multiple types of plastic, rubber, foam, and glass.

Metrics: *Point Error:* This metric measures the error of a given point within our reconstructions, by measuring the distance from this point to its nearest neighbor in the ground-truth point cloud (P_G). Formally, point error $P(x_i, P_G)$ is:

$$P(x_i, P_G) = \min_{x_g \in P_G} \|x_i - x_g\| \quad (14)$$

¹¹In practice, this field of view may limit the recoverable surface normals. We note that future systems can overcome this by using spotlight SAR to point the radar towards the scene, avoiding potentially unrecoverable normals.

¹²In practice, we compute the cost over a limited number of antennas to minimize the computation time. We remove all antenna locations which do not receive a sufficiently strong reflection from the scene, and randomly select 50 of the remaining locations.

where x_i & x_g are points in the reconstruction & ground-truth.

We aggregate this error across all points and experiments to measure the overall reconstruction accuracy.

Relative Point Error. This metric measures the point error relative to the object’s size. Formally, this is defined as the point error normalized by the diameter of the object:

$$RP(x_i, P_G, d_G) = \frac{P(x_i, P_G)}{d_G} \times 100\% \quad (15)$$

where $RP(x_i, P_G, d_G)$ is the relative point error, and d_G is the longest distance between two points on the object.

Shape Error (3D F-Score): We measure the similarity between the reconstructed and ground-truth shapes with the standard 3D F-Score [62], which balances precision (accuracy of predicted points) and recall (coverage of ground truth points). A point is accurate if it is within a threshold distance of the ground truth. Similarly, a ground truth point is covered if it is within the threshold distance of the reconstruction:

$$FS = \frac{2 PR RE}{PR + RE}, RE = \frac{1}{N_G} \sum_{j=1}^{N_G} \mathbb{1}_{d(x_j, P_m) < \tau}, PR = \frac{1}{N_m} \sum_{i=1}^{N_m} \mathbb{1}_{d(x_i, P_G) < \tau}$$

where FS , PR , RE , denote F-Score, precision and recall respectively. $\mathbb{1}$ is an indicator variable. P_m is the reconstructed point cloud. τ is the threshold distance.¹³ F-Score ranges from 0 to 1, with 1 denoting a high-accuracy reconstruction.

To evaluate only the difference in shape, we break down the total error into shape error and position error (see below). The shape error is obtained after subtracting the estimated position error as a single translation applied to all points in the reconstruction.

Position Error: We measure the vertical distance between the ground truth and reconstructed point clouds. Formally, we take the difference between the 80th percentile height in reconstruction and the 80th percentile ground-truth height:

$$T(P_m, P_G) = |\text{pcntl}(\{z_i | z_i \in P_m\}, 80) - \text{pcntl}(\{z_j | z_j \in P_G\}, 80)|$$

where z_i and z_j are the z (height) coordinates of points within P_m and P_G , respectively. $\text{pcntl}(\cdot, \cdot)$ is the percentile operator.

Cosine Similarity: To measure our estimated normal accuracy, we use the cosine similarity [45] to measure the similarity between two vectors. Here, 1 represents perfectly aligned vectors, and 0 represents perpendicular vectors.¹⁴ Formally:

$$S(\hat{\mathbf{n}}_i, \mathbf{n}_j) = |\hat{\mathbf{n}}_i \cdot \mathbf{n}_j| / (\|\hat{\mathbf{n}}_i\| \|\mathbf{n}_j\|) \quad (16)$$

where $\hat{\mathbf{n}}_i$ and \mathbf{n}_j are the estimated and ground-truth normals.

Baselines: We implemented two state-of-the-art baselines.

Backprojection [19]: Our first baseline reconstructs a 3D mmWave image of the object through standard backprojection imaging, and then selects the voxels that exceeds a certain threshold relative to the maximum image value. It uses the center of these voxels as points to reconstruct a 3D point cloud of the object. We selected the threshold which produces the highest median 3D F-Score across all objects.

Interferometric [21]: This baseline iteratively produces 2D SAR

¹³In our implementation, τ is 0.015m.

¹⁴Since a normal vector can point in two directions (into or out of the object), we flip ground-truth normals to match the nearest direction of the estimates— e.g., two opposite vectors (180° apart) have a cosine similarity=1.

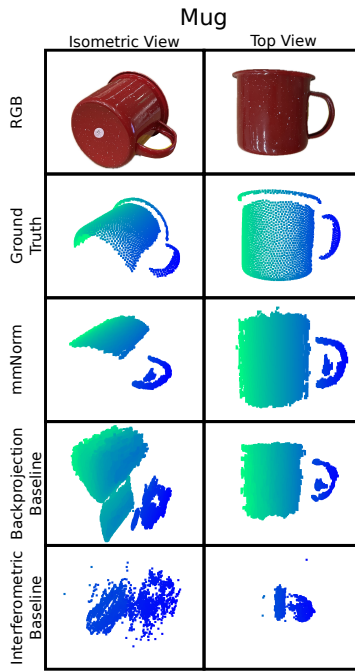


Figure 10: Qualitative Evaluation from three different NLOS experiments, visualized from an isometric and top view.

images of the target with small bandwidths, then compares the change in phase across frequency to derive the object’s depth. Since this method only estimates changes in depth, and requires a reference point to provide absolute depth, we offset the reconstruction by the average height (depth) of the high-power regions in the standard, 3D mmWave image.

Ground Truth: To obtain a ground-truth 3D reconstruction, we used the Intel Realsense D415 [30] depth camera on the robot wrist to capture a depth image from directly above the object.¹⁵ For NLOS experiments, we first captured the depth image in line-of-sight before placing the occlusion.¹⁶

6 Results

We report the results from 116 real-world experimental trials.

6.1 Qualitative Results

First, we provide qualitative performance results for mmNorm and the baselines across three of the NLOS experiments.

Fig. 10 shows the qualitative results, including the RGB (1st row), ground truth point cloud (2nd row), mmNorm’s reconstruction (3rd row), the *Backprojection* baseline’s reconstruction (4th row), and the *Interferometric* baseline’s reconstruction (5th row). The color of the points denotes the x coordinate of that point. To ensure consistency, all point clouds in a column are plotted from the same angle. We show experiments for a mug, chips can, and power drill, visualized from both an isometric and top view. We note the following:

- Let us first consider the chips can (middle). Looking at the isometric view, we can see that mmNorm’s reconstructed surface closely matches the ground truth in its curvature. In contrast, the

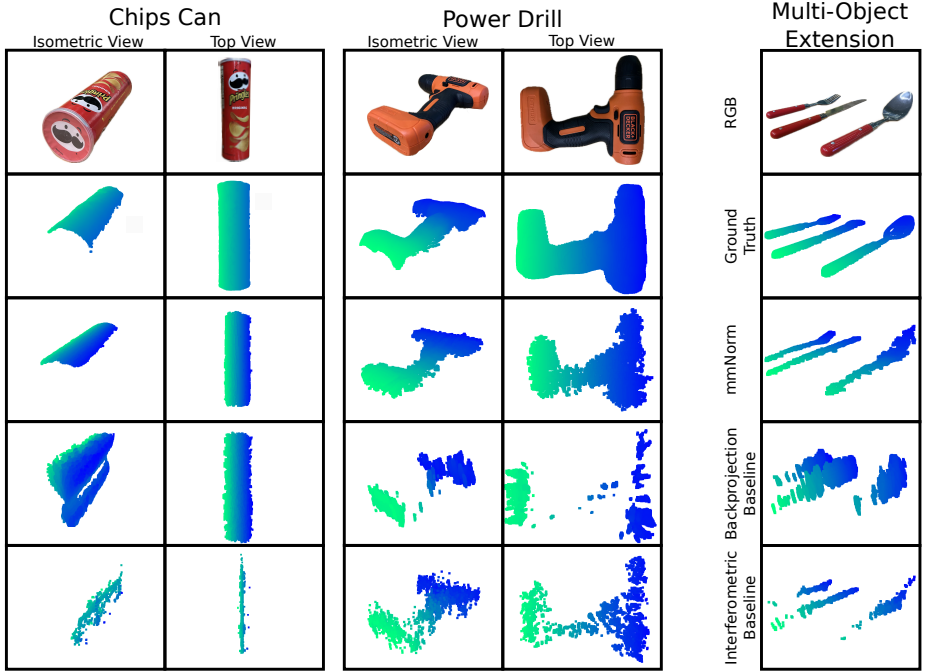


Figure 11: Multi-Objects

Backprojection baseline vastly overestimates the voxels that correspond to the surface to the extent that one cannot identify that it is curved altogether. Furthermore, the *Interferometric* baseline is very sparse, making it difficult to delineate the surface.¹⁷ The same can be seen in the isometric view of the mug, whereby mmNorm succeeds in capturing the surface curvature, but both of the baselines fail. These show how mmNorm significantly outperforms the baselines in surface reconstruction.

- Let us next consider the top view of the mug. Here, we can see that both mmNorm and the *Backprojection* baseline closely match the ground truth (with mmNorm slightly outperforming the baseline). This is expected, since the synthetic aperture produces a high horizontal resolution, which allows for accurate 2D reconstruction in both mmNorm and the baselines. However, when viewed from the side, the baseline will have points spread across a large depth range due to the radar’s limited depth resolution, while mmNorm achieves accurate 3D reconstruction. On the other hand, the *Interferometric* baseline is again sparse.
- mmNorm can accurately reconstruct complex surfaces like the mug and power drill. For example, it captures both the handle and the curve of the mug, which has complicated surface normals. This shows the benefit of mmNorm’s techniques for generating reconstructions of objects with complex geometries.
- mmNorm also succeeds across various materials (metal, plastic, cardboard, composite) and textures, as seen here.

6.1.1 Extension to Multiple Objects. Next, we demonstrate an extension of mmNorm for multiple objects. Here, we placed three

¹⁵For high optical specularity (e.g., a shiny spoon), the depth image may be noisy. We align a ground-truth mesh (provided by the YCB [8] dataset, which the MITO dataset builds on) to the depth image using Iterative Closest Point, and use the top mesh surface as ground truth.

¹⁶A few experiments reconstructed the cardboard occlusion and the hidden object. Since the occlusion is not in our ground-truth, we removed points above a set height, corresponding to the occlusion (for mmNorm and the baselines).

¹⁷Here, the *Interferometric* baseline is sparse since it applies a single threshold to determine which voxels in the 2D image are considered within the object. The threshold was selected to maximize the median & 90th percentile performance of the baseline. However, since our evaluation covers a large diversity of objects, some objects are under-thresholded and thus contain fewer points. In other cases, objects such as the power drill do not appear sparse (but still exhibit poor 3D reconstruction). A similar phenomenon can be observed in the *Backprojection* baseline.

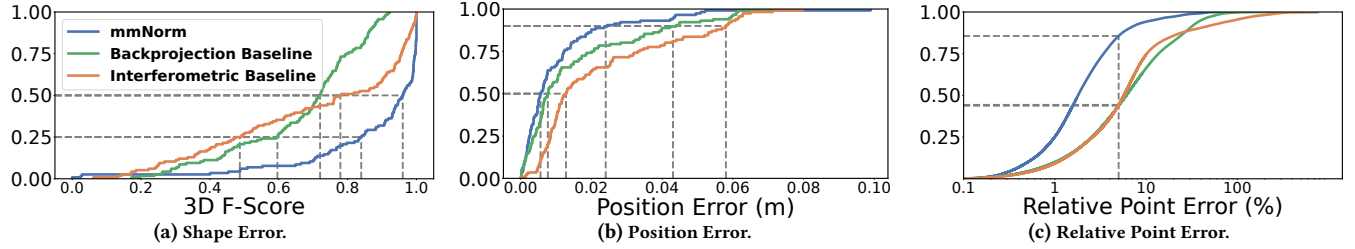


Figure 12: Performance Results. a) Shape, b) position, and c) relative point error for mmNorm (blue), Backprojection (green), and Interferometric (orange).

objects - a fork, knife, and spoon - in the environment. Fig. 11 shows results for mmNorm and the baselines. Here, mmNorm’s reconstruction closely match the ground-truth curvatures, while the baseline reconstructions contain significant distortions. This highlights mmNorm’s potential for more complicated scenarios containing multiple objects.

6.2 Performance Results

6.2.1 Shape Error. To evaluate the shape error, we compute the 3D F-Score (defined in §5) for mmNorm and the baselines.

Fig. 12a plots a CDF of the shape error for mmNorm (blue), the *Backprojection* baseline (green), and the *Interferometric* baseline (orange). The dashed lines show the 50th and 25th percentiles. Note:

- mmNorm achieves a median F-score of 96%, in contrast to only 72% and 78% for the *Backprojection* and *Interferometric* baselines. This shows the benefit of mmNorm’s techniques for enabling accurate reconstructions.
- Similarly, we compare the 25th percentile performances. Since larger F-Scores are better, the 25th percentile demonstrates the robustness (or lack thereof) to challenging scenarios. mmNorm achieves a 25th percentile of 84%, while the *Backprojection* and the *Interferometric* baselines only achieve 60% and 49%, respectively. This demonstrates the robustness of mmNorm’s techniques for reconstructing high-accuracy shapes in challenging scenarios.

6.2.2 Position Error. We evaluate position error defined in §5.

Fig. 12b plots a CDF of the position error in meters for mmNorm (blue), *Backprojection* (green), and *Interferometric* (orange). Dashed lines show the 50th/90th percentiles. We note the following:

- The *Backprojection* and *Interferometric* baselines have a median position error of 0.8 cm and 1.3 cm, respectively. mmNorm achieves a median position error of 0.6 cm. Note that this position error is *in addition* to the shape error. It shows that mmNorm not only exceeds the shape accuracy of state-of-the-art baselines, but also matches the median position accuracy of the best performing baseline.
- The baselines have a 90th percentile position error of 4.3 cm & 5.8 cm, compared to mmNorm’s 2.4 cm. Thus, mmNorm achieves an almost 2x improvement in the 90th percentile over the baselines, showing the benefit of its techniques for producing reconstructions with accurate absolute depth.

6.2.3 Relative Point Error. Next, we measure the error of the individual points relative to the object’s size by measuring the relative point error (defined in §5).

Fig. 12c plots a CDF of the relative point error in log scale for mmNorm (blue), *Backprojection* (green), and *Interferometric* (orange). The dashed lines show what percentage of points within the reconstructions achieve an error less than 5% of the object’s size. We

note that both baselines have only 44% of their points with an error within 5% of the object’s size, in contrast to 85% for mmNorm. This reinforces mmNorm’s significant improvement over the baselines.

6.3 Microbenchmarks

We performed microbenchmark experiments to understand the impact of various factors on mmNorm’s performance.

6.3.1 Surface Normal Vector Field Accuracy. Our first microbenchmark evaluates the accuracy of mmNorm’s surface normal vector field produced in §2. To do so, we produce ground-truth surface normal vector fields by: 1) aligning the ground-truth object mesh (provided in the YCB dataset [8], which the MITO dataset [18] builds on) with the camera’s depth image using ICP [5], 2) using the mesh to produce a ground-truth, 3D SDF of the object [69], and 3) taking the gradient of the SDF to produce the ground-truth normal vector field [55, 66].¹⁸ For each normal estimated by mmNorm, we measure the cosine-similarity (see §5) between the ground-truth and estimated normals. We aggregate across all normal estimates.¹⁹

We compare this to the performance of normals that would be produced using the reconstructions of the *Backprojection* and *Interferometric* baselines. To do so, we use a standard point-cloud normal estimation method [80] to estimate the normal vector for each point in the baseline reconstructions. We then measure the cosine-similarity for every normal.²⁰

Fig. 13 plots a CDF of the cosine-similarity for mmNorm (blue), *Backprojection* (green), and *Interferometric* (orange). The dashed lines show the 50th/25th percentile. We note that:

- mmNorm achieves a 50th and 25th percentile cosine-similarity of 0.99 and 0.94, respectively. This demonstrates that mmNorm is capable of producing high-accuracy normal vectors.
- In contrast, *Backprojection* achieves a 50th and 25th percentile of 0.54 and 0.22, and *Interferometric* achieves only 0.66 and 0.36, respectively. This shows that state-of-the-art approaches cannot accurately estimate surface normals.

6.3.2 Benefit of Isosurface Optimization. Next, we evaluate the benefit of mmNorm’s isosurface optimization technique (per §4), by comparing mmNorm’s performance with two partial implementations. These implementations still estimate normal vectors (§2) and produce RSDF components (§3) in the same way. However, they do not leverage the isosurface optimization. Instead, the first partial implementation simply selects the isosurface in the center (vertically) of each RSDF component. To do so, it selects the unknown RSDF constant (C_n) as the average of the maximum and minimum RSDF values, as $C_n = (\max(f_n^R) + \min(f_n^R)) / 2$. The second partial implementation selects an isosurface weighted by the

¹⁸We interpolate the ground-truth vector field to match mmNorm.

¹⁹For this microbenchmark, we remove objects with no valid mesh file.

²⁰Again, we interpolate the ground-truth normals at each point.

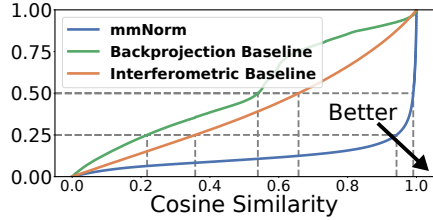


Figure 13: Normal Field Accuracy. CDF of cosine similarity of normal estimates for mmNorm.

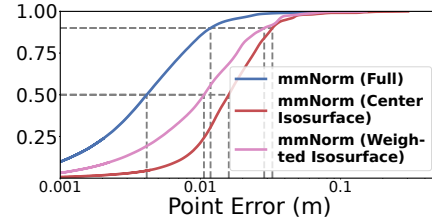


Figure 14: Benefit of Optimization. CDF of point error for mmNorm(blue), and partial implementations selecting the center (red), and weighted center (pink).

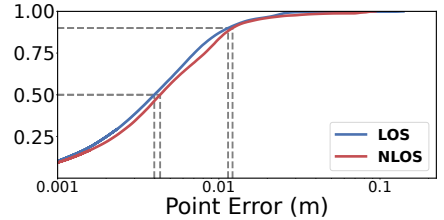


Figure 15: Impact of Non-Line-of-Sight. CDF of point error in LOS (blue) and NLOS (red).

mmWave SAR image magnitude. Specifically, we discretely sample isosurfaces every $\lambda/2 \approx 1.9$ mm, and compute the total SAR image magnitude across each isosurface. We then compute the average isosurface weighted by the total SAR image power. Formally:

$$C_n = \frac{\sum_{c=\min(f_n^R)}^{\max(f_n^R)} c w_c}{\sum_{c=\min(f_n^R)}^{\max(f_n^R)} w_c}, \quad w_c = \sum_{v_i \in (f_n^R - c=0)} |S(v_i)|$$

where w_c are the weighting values based on mmWave image.

Fig. 14 plots a CDF of the overall point error in log scale for mmNorm (blue), the partial implementation using the RSDF center (red), and the partial implementation using weighted centers (pink). The dashed lines show the median and 90th percentile. We note that the partial implementation using RSDF centers achieves a median and 90th percentile error of 1.6 cm and 3.3 cm, respectively, and the partial implementation using weighted centers achieves 1.1 cm and 2.9 cm, respectively. In contrast, mmNorm achieves a roughly 3x and 2.5x improvement, with a median and 90th percentile error of 0.4 cm and 1.2 cm.

6.3.3 Impact of Non-Line-of-Sight. Next, we evaluate how NLOS impacts mmNorm by comparing the performance in LOS and NLOS scenarios (when fully occluded by a layer of cardboard).

Fig. 15 plots a CDF of the overall point error in log scale for mmNorm in LOS (blue) and NLOS (red). The dashed lines show the median and 90th percentile. We note that in LOS, mmNorm achieves a median and 90th percentile of 0.39 cm and 1.1 cm, respectively. In NLOS conditions, mmNorm achieves a median and 90th percentile error of 0.43 cm and 1.2 cm, respectively. This shows that mmNorm is capable of producing high-accuracy reconstructions in NLOS, with a negligible performance difference compared to LOS.²¹

7 Related Work

mmWave-based 3D Object Reconstruction. Previous research in mmWave reconstruction falls in two main categories: first-principles and machine learning based approaches.

Within first-principle-based methods, the most common approach involves applying ray-tracing based imaging algorithms (e.g., range migration algorithm or backprojection) to generate 3D mmWave images. Then, this image is directly used for occupancy detection (e.g., by selecting all voxels that exceed a power threshold) [15, 19, 37, 38, 40, 52]. As shown in our results, mmNorm significantly outperforms this method (the *Backprojection* baseline) when using commercially available bandwidth. In principle, one could rely on significantly larger bandwidth (≥ 10 GHz) to obtain more accurate 3D object reconstructions [15, 23, 37, 38, 40, 52].

²¹Note that similar to any mmWave system, while the SNR would decrease with thicker occlusions, this can be offset with higher transmit power.

However, such bandwidth is reserved only for government and military use, making it unsuitable for commercial applications.

To overcome the bandwidth limitations, some works have proposed interferometric methods, which rely primarily on the phase. Existing approaches have only demonstrated imaging a handful of metallic objects in anechoic chamber [20–23] and do not generalize well. Indeed, our results show that mmNorm significantly outperform the *Interferometric* baseline [21], which is a state-of-the-art system in this space. Finally, mmNorm is also related to [81], which leverages incoherent methods to estimate an object’s 2D surface normals and perform coarse reconstruction. In contrast, mmNorm develops coherent methods for 3D surface normal estimation and object reconstruction, producing significantly finer reconstructions of smaller-scale objects and features.

The second category utilizes machine learning to produce high resolution reconstructions using a limited, commercially available bandwidth. These works focus on a specific category (or limited categories) of objects, and use advanced learning models to produce reconstructions beyond the radar resolution. For example, there has been work on reconstructing human bodies [9–12, 28, 35, 70, 75–78], human faces [74], vehicles [24, 57–59, 61], and scene-level features (e.g., walls, furniture, etc) [7, 14, 36, 42, 48, 54]. However, these works are limited in that they can only produce 3D reconstructions for objects within their specific category. Also, enabling such learning-based approaches requires exhaustive training data. In contrast, mmNorm uses an entirely first-principles-based approach for mmWave 3D object reconstruction (for objects orders of magnitude smaller than cars, humans, etc). Thus, mmNorm generalizes to completely unseen objects and environments without requiring exhaustive training data.

Surface Normal Characterization. Certain perception tasks require characterizing a surface using its normals. Past work has done this by first reconstructing human or scene-level features using RF signals, then estimating the normals (in a straightforward fashion or using machine learning) [27, 36, 46, 70]. This is fundamentally different than mmNorm which estimates surface normals from first principles, then uses them to reconstruct the surface with high accuracy. Indeed, our §6.3.1 micro-benchmark shows that mmNorm is >2.5x more accurate than such methods, which first reconstruct the surface then use it to estimate normals.

Optical-based 3D Object Reconstruction. Optical-based 3D reconstruction has been extensively studied over the past decade, with prior work leveraging LiDAR [56, 67, 71] or RGB [51, 60, 73] scans of an object to produce 3D reconstructions. However, these methods are limited to the line-of-sight and cannot reconstruct fully-occluded objects (e.g., inside boxes, behind obstacles, or covered by

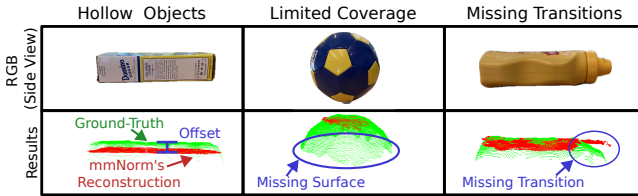


Figure 16: Limitations. Examples of various limitations of mmNorm.

clutter). This is because they rely on visible light or near-infrared, which cannot traverse through occlusions. In contrast, mmNorm enables NLOS 3D reconstruction by leveraging mmWave signals, which can traverse many everyday occlusions.

There have also been a small number of works that investigate reflecting light around the corner to reconstruct hidden objects [13, 26, 29, 34, 65]. However, this approach cannot reconstruct fully occluded objects (e.g., within a closed box). Also, these works rely on expensive equipment and/or high-powered lasers which are unsafe for human exposure.

8 Limitations

We highlight few limitations and avenues to overcome them:

Metal Occlusions. Similar to existing mmWave imaging systems, mmNorm cannot reconstruct objects hidden behind metal (or very thick) occlusions.

Hollow Objects. In the case of a hollow (and non-metallic) object, such as an empty cardboard box, the mmWave signals may traverse through the object and the radar may receive reflections from both the top and bottom surfaces. However, since mmNorm only produces one isosurface per RSDF component, it cannot reconstruct both surfaces. For example, in the first column of Fig. 16 we show an RGB image, ground truth point cloud (green), and mmNorm’s reconstruction (red) for an empty box. Here, mmNorm’s reconstruction does not align with the top (or bottom) of the box.

It would be interesting future work to extend mmNorm to detect these scenarios and produce reconstructions for both the top and bottom surfaces of narrow, hollow objects.

Limited Coverage. mmNorm inherits the existing coverage limitation of synthetic aperture radar. Specifically, recall from §2.1 that a mmWave image is only able to capture portions of the surface where the normal points within the aperture. This prevents mmNorm from reconstructing the normals (and thus the surface) for parts of the object where the normal points outside the aperture. We show an example of a mini soccer ball in Fig. 16 (2nd col). Due to the limited aperture, mmNorm is only able to reconstruct the top portion of the object (where normals point within the aperture).

It would be interesting future work to investigate other aperture lengths and shapes to improve the surface coverage of mmNorm, as well as to leverage deep learning methods for completing an object’s shape from a partial reconstruction.

Missing Object Transitions. In some cases, mmNorm is unable to capture sharp transitions in the object’s shape. We show this through an example of a mustard bottle in Fig. 16 (3rd col). While the reconstruction closely matches at many points on the object, it deviates at the bottle’s cap, as shown within the blue circle. This is because mmNorm is unable to recover the surface normals corresponding with the sharp transition of the object (due to the same coverage problem described above). In many cases, this is overcome by leveraging different RSDF components to separate the different

object surfaces. However, in this case, both the main body and the cap are very close to each other. Thus, they are selected to be within one RSDF component. This prevents mmNorm from separately optimizing their isosurfaces, resulting in the reconstruction error shown. It would be interesting future work to identify this case (e.g., by detecting sharp changes in signal response or through a mmWave segmentation network) and split the RSDF into separate components so their isosurfaces can be optimized independently, allowing for better reconstruction.

Internal Object Multipath: mmNorm’s normal estimates may be impacted by multipath within an object. We believe it would be interesting future work to investigate the impact of this phenomenon, and incorporate it into the normal estimation or isosurface optimization to improve the object reconstruction.

Computational Complexity and Scanning Time: Finally, future work can investigate avenues for enabling real-time scanning and computation. First, we envision future work can leverage faster, integrated scanners, similar to those used in mmWave airport scanners which can scan a large aperture in a few seconds (despite using a much larger bandwidth than our system which is not commercially available). Second, since many steps of mmNorm’s algorithms are highly parallelizable, mmNorm could benefit from similar optimizations to existing SAR image computations (e.g., GPU, hardware acceleration, etc) [17, 49] to enable future real-time computation.

9 Conclusion & Future Opportunities

We presented mmNorm, a fundamentally new method for NLOS 3D object reconstruction via mmWave surface normal estimation, opening future work along multiple dimensions.

For example, it would be interesting to investigate how mmNorm’s methods may bring benefit to *larger objects or scene-level reconstructions*. By leveraging surface normal estimates in these scenarios, it may be possible to further enhance autonomous vehicle sensing or RF-SLAM systems.

Also, we imagine that future work could enable *camera-quality NLOS reconstructions*. Similar to how past work has enabled lidar-quality scene reconstructions from long-range mmWave measurements [36], we envision that one could leverage mmNorm’s reconstructions as input to a deep learning model to produce photo-realistic reconstructions.

Further, we believe mmNorm can *enable novel downstream tasks*. For example, we envision a new domain of NLOS robotic systems which can directly locate and grasp objects which are hidden from view (i.e., objects within boxes of packing peanuts or hidden in dark locations). Furthermore, future work could investigate combining arrays on AR headsets with human motion to reconstruct surrounding objects and display high-resolution hidden models to the user. Finally, high-accuracy reconstruction could enable new capabilities in areas such as gesture recognition, NLOS quality control in shipping and logistics, and hidden object classification and completion.

More broadly, we hope that this work motivates a new direction for high-accuracy, non-line-of-sight 3D reconstruction.

Acknowledgments. We thank the anonymous reviewers and the Signal Kinetics group for their help and feedback. This research is sponsored by NSF (Award #2313234) and the MIT Media Lab. Tara Boroushaki is supported by the Microsoft PhD fellowship.

References

- [1] 2021. mmWave Radar Radome Design Guide. <https://www.ti.com/lit/an/swra705/swra705.pdf>. Texas Instruments.
- [2] 2023. TI DCA1000EVM. <https://www.ti.com/tool/DCA1000EVM>.
- [3] 2023. TI IWR1443Boost. <https://www.ti.com/product/IWR1443#tech-docs>.
- [4] 2024. 5G mmWave Channel Modeling with Diffuse Scattering in an Office Environment . <https://www.remcom.com/resources/examples/5g-mmwave-channel-modeling-with-diffuse-scattering-in-an-office-environment>. Remcom.
- [5] 2024. ICP registration. https://www.open3d.org/docs/release/tutorial/pipelines/icp_registration.html.
- [6] Daniel Arnitz, Claire M Watts, Andreas Pedross-Engel, and Matthew S Reynolds. 2022. A portable K-band (24 GHz) 3-D millimeter wave imaging system for detecting and dimensioning hidden objects. In *Passive and Active Millimeter-Wave Imaging XXV*, Vol. 12111. SPIE, 38–42.
- [7] Pingping Cai and Sanjib Sur. 2023. Millipcd: Beyond traditional vision indoor point cloud generation via handheld millimeter-wave devices. *Proceedings of the ACM on Interactive, Mobile, Wearable and Ubiquitous Technologies* 6, 4 (2023), 1–24.
- [8] Berk Calli, Arjun Singh, James Bruce, Aaron Walsman, Kurt Konolige, Siddhartha Srinivasa, Pieter Abbeel, and Aaron M Dollar. 2017. Yale-CMU-Berkeley dataset for robotic manipulation research. *The International Journal of Robotics Research* 36, 3 (2017), 261–268. doi:10.1177/0278364917700714 arXiv:<https://doi.org/10.1177/0278364917700714>
- [9] Anjun Chen, Xiangyu Wang, Kun Shi, Yuchi Huo, Jiming Chen, and Qi Ye. 2024. Towards Weather-Robust 3D Human Body Reconstruction: Millimeter-Wave Radar-Based Dataset, Benchmark, and Multi-Modal Fusion. *IEEE Transactions on Circuits and Systems for Video Technology* (2024).
- [10] Anjun Chen, Xiangyu Wang, Kun Shi, Shaohao Zhu, Bin Fang, Yingfeng Chen, Jiming Chen, Yuchi Huo, and Qi Ye. 2023. Immfusion: Robust mmwave-rgb fusion for 3d human body reconstruction in all weather conditions. In *2023 IEEE International Conference on Robotics and Automation (ICRA)*. IEEE, 2752–2758.
- [11] Anjun Chen, Xiangyu Wang, Zhi Xu, Kun Shi, Yan Qin, Yuchi Huo, Jiming Chen, and Qi Ye. 2024. AdaptiveFusion: Adaptive Multi-Modal Multi-View Fusion for 3D Human Body Reconstruction. *arXiv preprint arXiv:2409.04851* (2024).
- [12] Anjun Chen, Xiangyu Wang, Shaohao Zhu, Yanxu Li, Jiming Chen, and Qi Ye. 2022. mmbbody benchmark: 3d body reconstruction dataset and analysis for millimeter wave radar. In *Proceedings of the 30th ACM International Conference on Multimedia*, 3501–3510.
- [13] Wenzheng Chen, Simon Daneau, Fahim Mannan, and Felix Heide. 2019. Steady-state non-line-of-sight imaging. In *Proceedings of the IEEE/CVF Conference on Computer Vision and Pattern Recognition*, 6790–6799.
- [14] Yuwei Cheng, Jingran Su, Mengxin Jiang, and Yimin Liu. 2022. A novel radar point cloud generation method for robot environment perception. *IEEE Transactions on Robotics* 38, 6 (2022), 3754–3773.
- [15] R Trevor Clark, Stephanie L McDaid, and David M Sheen. 2024. Rotational millimeter-wave shoe scanner using the discrete Fourier transform for backprojection-based image reconstruction. In *Radar Sensor Technology XXVIII*, Vol. 13048. SPIE, 248–254.
- [16] Federal Communications Commission. 2003. FCC Opens 70, 80, and 90 GHz Spectrum Bands for Deployment of Broadband "Millimeter Wave" Technologies. <https://www.fcc.gov/document/fcc-opens-70-80-and-90-ghz-spectrum-bands-deployment-broadband>
- [17] Helena Cruz, Mário Véstias, José Monteiro, Horácio Neto, and Rui Policarpo Duarte. 2022. A Review of Synthetic-Aperture Radar Image Formation Algorithms and Implementations: A Computational Perspective. *Remote Sensing* 14, 5 (2022). doi:10.3390/rs14051258
- [18] Laura Dodds, Tara Boroushaki, Cusuh Ham, and Fadel Adib. 2025. MITO: A Millimeter-Wave Dataset and Simulator for Non-Line-of-Sight Perception. *arXiv:2502.10259 [cs.CV]* <https://arxiv.org/abs/2502.10259>
- [19] Laura Dodds, Hailan Shanbhag, Junfeng Guan, Saurabh Gupta, and Haitham Hassanieh. 2024. Around the Corner mmWave Imaging in Practical Environments. In *Proceedings of the 30th Annual International Conference on Mobile Computing and Networking*, 1–15.
- [20] Jingkun Gao, Bin Deng, Yuliang Qin, Xiang Li, and Hongqiang Wang. 2019. Point cloud and 3-D surface reconstruction using cylindrical millimeter-wave holography. *IEEE Transactions on Instrumentation and Measurement* 68, 12 (2019), 4765–4778.
- [21] Jingkun Gao, Yuliang Qin, Bin Deng, Hongqiang Wang, and Xiang Li. 2017. A novel method for 3-D millimeter-wave holographic reconstruction based on frequency interferometry techniques. *IEEE Transactions on Microwave Theory and Techniques* 66, 3 (2017), 1579–1596.
- [22] Jingkun Gao, Yuliang Qin, Bin Deng, Hongqiang Wang, and Xiang Li. 2018. Novel efficient 3D short-range imaging algorithms for a scanning 1D-MIMO array. *IEEE Transactions on Image Processing* 27, 7 (2018), 3631–3643.
- [23] Borja Gonzalez-Valdes, Yuri Alvarez-Lopez, Jose Angel Martinez-Lorenzo, Fernando Las Heras Andres, and Carey Rappaport. 2013. On the use of improved imaging techniques for the development of a multistatic three-dimensional millimeter-wave portal for personnel screening. *Progress In Electromagnetics Research* 138 (2013), 83–98.
- [24] Junfeng Guan, Sohrab Madani, Suraj Jog, Saurabh Gupta, and Haitham Hassanieh. 2020. Through fog high-resolution imaging using millimeter wave radar. In *Proceedings of the IEEE/CVF Conference on Computer Vision and Pattern Recognition*, 11464–11473.
- [25] Qijia Guo, Jie Liang, Tianying Chang, and Hong-Liang Cui. 2019. Millimeter-wave imaging with accelerated super-resolution range migration algorithm. *IEEE Transactions on Microwave Theory and Techniques* 67, 11 (2019), 4610–4621.
- [26] Otkrist Gupta, Thomas Willwacher, Andreas Velten, Ashok Veeraraghavan, and Ramesh Raskar. 2012. Reconstruction of hidden 3D shapes using diffuse reflections. *Optics express* 20, 17 (2012), 19096–19108.
- [27] William D Harcourt, David G Macfarlane, and Duncan A Robertson. 2024. 3D terrain mapping and filtering from coarse resolution data cubes extracted from real-aperture 94 GHz radar. *IEEE Transactions on Geoscience and Remote Sensing* (2024).
- [28] Kareeb Hasan, Beng Oh, Nithurshan Nadarajah, and Mehmet Rasit Yuce. 2024. mm-CasGAN: A cascaded adversarial neural framework for mmWave radar point cloud enhancement. *Information Fusion* 108 (2024), 102388.
- [29] Felix Heide, Lei Xiao, Wolfgang Heidrich, and Matthias B Hullin. 2014. Diffuse mirrors: 3D reconstruction from diffuse indirect illumination using inexpensive time-of-flight sensors. In *Proceedings of the IEEE Conference on Computer Vision and Pattern Recognition*, 3222–3229.
- [30] Intel RealSense. 2019. <https://www.intelrealsense.com>.
- [31] Mohinder Jankiraman. 2018. *FMCW radar design*. Artech House.
- [32] Yue Jiang, Dantong Ji, Zhizhong Han, and Matthias Zwicker. 2020. Sdfdiff: Differentiable rendering of signed distance fields for 3d shape optimization. In *Proceedings of the IEEE/CVF conference on computer vision and pattern recognition*, 1251–1261.
- [33] Taenam Kim and Kyungyong Chwa. 1986. Parallel algorithms for a depth first search and a breadth first search. *International journal of computer mathematics* 19, 1 (1986), 39–54.
- [34] Ahmed Kirmani, Tyler Hutchison, James Davis, and Ramesh Raskar. 2011. Looking around the corner using ultrafast transient imaging. *International journal of computer vision* 95 (2011), 13–28.
- [35] Hao Kong, Haoxin Lyu, Jiadi Yu, Linghe Kong, Junlin Yang, Yanzhi Ren, Hongbo Liu, and Yi-Chao Chen. 2024. mmHand: 3D Hand Pose Estimation Leveraging mmWave Signals. In *2024 IEEE 44th International Conference on Distributed Computing Systems (ICDCS)*. IEEE, 1062–1073.
- [36] Haowen Lai, Gaoxiang Luo, Yifei Liu, and Mingmin Zhao. 2024. Enabling Visual Recognition at Radio Frequency. In *Proceedings of the 30th Annual International Conference on Mobile Computing and Networking*, 388–403.
- [37] Jaime Laviada, Ana Arbolea-Arbolea, Yuri Álvarez, Borja González-Valdés, and Fernanda Las-Heras. 2017. Multiview three-dimensional reconstruction by millimetre-wave portable camera. *Scientific reports* 7, 1 (2017), 6479.
- [38] Jaime Laviada, Miguel Lopez-Portugues, Ana Arbolea-Arbolea, and Fernando Las-Heras. 2018. Multiview mm-wave imaging with augmented depth camera information. *IEEE Access* 6 (2018), 16869–16877.
- [39] CH Li and Peter Kwong-Shun Tam. 1998. An iterative algorithm for minimum cross entropy thresholding. *Pattern recognition letters* 19, 8 (1998), 771–776.
- [40] Bo Lin, Chao Li, Yicai Ji, Xiaojun Liu, and Guangyou Fang. 2023. A Millimeter-Wave 3D Imaging Algorithm for MIMO Synthetic Aperture Radar. *Sensors* 23, 13 (2023), 5979.
- [41] Ting Liu, Yao Zhao, Yunchao Wei, Yufeng Zhao, and Shikui Wei. 2019. Concealed Object Detection for Activate Millimeter Wave Image. *IEEE Transactions on Industrial Electronics* 66, 12 (2019), 9909–9917. doi:10.1109/TIE.2019.2893843
- [42] Chris Xiaoxuan Lu, Stefano Rosa, Peijun Zhao, Bing Wang, Changhao Chen, John A Stankovic, Niki Trigoni, and Andrew Markham. 2020. See through smoke: robust indoor mapping with low-cost mmwave radar. In *Proceedings of the 18th International Conference on Mobile Systems, Applications, and Services*, 14–27.
- [43] Jonathan S Lu, Patrick Cabrol, Daniel Steinbach, and Ravikumar V Pragada. 2013. Measurement and characterization of various outdoor 60 GHz diffracted and scattered paths. In *MILCOM 2013-2013 IEEE Military Communications Conference*. IEEE, 1238–1243.
- [44] Aditya Varma Muppala, Adib Y Nashashibi, Ehsan Afshari, and Kamal Sarabandi. 2024. Fast-Fourier Time-Domain SAR Reconstruction for Millimeter-Wave FMCW 3-D Imaging. *IEEE Transactions on Microwave Theory and Techniques* (2024).
- [45] Hieu V. Nguyen and Li Bai. 2011. Cosine Similarity Metric Learning for Face Verification. In *Computer Vision – ACCV 2010*, Ron Kimmel, Reinhard Klette, and Akihiro Sugimoto (Eds.). Springer Berlin Heidelberg, Berlin, Heidelberg, 709–720.
- [46] S Pawliczek, R Herschel, and N Pohl. 2019. 3D millimeter wave screening for metallic surface defect detection. In *2019 16th European Radar Conference (EuRAD)*. IEEE, 113–116.
- [47] Andreas Pedross-Engel, Claire M Watts, and Matthew S Reynolds. 2021. A two-sided, reflection-based K-Band 3-D millimeter-wave imaging system with image beat pattern mitigation. *IEEE Transactions on Microwave Theory and Techniques*

- 69, 11 (2021), 5045–5056.
- [48] Akarsh Prabhakara, Tao Jin, Arnav Das, Gantavya Bhatt, Lilly Kumari, Elahe Soltanaghi, Jeff Bilmes, Swaran Kumar, and Anthony Rowe. 2023. High resolution point clouds from mmwave radar. In *2023 IEEE International Conference on Robotics and Automation (ICRA)*. IEEE, 4135–4142.
- [49] Dan Pritsker. 2015. Efficient Global Back-Projection on an FPGA. In *2015 IEEE Radar Conference (RadarCon)*. 0204–0209. doi:10.1109/RADAR.2015.7130996
- [50] Ming-Hao Ren, Xi Liao, Jihua Zhou, Yang Wang, Yu Shao, Shasha Liao, and Jie Zhang. 2020. Diffuse Scattering Directive Model Parameterization Method for Construction Materials at mmWave Frequencies. *International Journal of Antennas and Propagation* 2020, 1 (2020), 1583854. doi:10.1155/2020/1583854 arXiv:<https://onlinelibrary.wiley.com/doi/pdf/10.1155/2020/1583854>
- [51] Ruizhi Shao, Zerong Zheng, Hongwen Zhang, Jingxiang Sun, and Yebin Liu. 2022. Diffustereo: High quality human reconstruction via diffusion-based stereo using sparse cameras. In *European Conference on Computer Vision*. Springer, 702–720.
- [52] David M Sheen and Thomas E Hall. 2011. Calibration, reconstruction, and rendering of cylindrical millimeter-wave image data. In *Passive Millimeter-Wave Imaging Technology XIV*, Vol. 8022. SPIE, 123–134.
- [53] Ruiyi Shen and Yasaman Ghasempour. 2023. Scattering from Rough Surfaces in 100+ GHz Wireless Mobile Networks: From Theory to Experiments. In *Proceedings of the 29th Annual International Conference on Mobile Computing and Networking (Madrid, Spain) (ACM MobiCom '23)*. Association for Computing Machinery, New York, NY, USA, Article 92, 15 pages. doi:10.1145/3570361.3613306
- [54] Akash Deep Singh, Yunhao Ba, Ankur Sarker, Howard Zhang, Achuta Kadambi, Stefano Soatto, Mani Srivastava, and Alex Wong. 2023. Depth estimation from camera image and mmwave radar point cloud. In *Proceedings of the IEEE/CVF Conference on Computer Vision and Pattern Recognition*. 9275–9285.
- [55] Herman Hansson Söderlund, Alex Evans, and Tomas Akenine-Möller. 2022. Ray Tracing of Signed Distance Function Grids. *Journal of Computer Graphics Techniques* Vol 11, 3 (2022).
- [56] Su Sun, Cheng Zhao, Yuliang Guo, Ruoyu Wang, Xinyu Huang, Yingjie Victor Chen, and Liu Ren. 2024. Behind the Veil: Enhanced Indoor 3D Scene Reconstruction with Occluded Surfaces Completion. In *Proceedings of the IEEE/CVF Conference on Computer Vision and Pattern Recognition*. 12744–12753.
- [57] Yue Sun, Zhuoming Huang, Honggang Zhang, Zhi Cao, and Deqiang Xu. 2021. 3DRIMR: 3D reconstruction and imaging via mmWave radar based on deep learning. In *2021 IEEE International Performance, Computing, and Communications Conference (IPCCC)*. IEEE, 1–8.
- [58] Yue Sun, Zhuoming Huang, Honggang Zhang, and Xiaohui Liang. 2022. 3D reconstruction of multiple objects by mmWave radar on UAV. In *2022 IEEE 19th International Conference on Mobile Ad Hoc and Smart Systems (MASS)*. IEEE, 491–495.
- [59] Yue Sun, Honggang Zhang, Zhuoming Huang, and Benyuan Liu. 2021. Deeppoint: A deep learning model for 3d reconstruction in point clouds via mmwave radar. *arXiv preprint arXiv:2109.09188* (2021).
- [60] Stanislaw Szumanowicz, Christian Rupprecht, and Andrea Vedaldi. 2024. Splatter image: Ultra-fast single-view 3d reconstruction. In *Proceedings of the IEEE/CVF Conference on Computer Vision and Pattern Recognition*. 10208–10217.
- [61] Bin Tan, Zhixiong Ma, Xichan Zhu, Sen Li, Lianqing Zheng, Sihan Chen, Libo Huang, and Jie Bai. 2022. 3-D object detection for multiframe 4-D automotive millimeter-wave radar point cloud. *IEEE Sensors Journal* 23, 11 (2022), 11125–11138.
- [62] Maxim Tatarchenko*, Stephan R. Richter*, René Ranftl, Zhuwen Li, Vladlen Koltun, and Thomas Brox. 2019. What Do Single-view 3D Reconstruction Networks Learn? *CVPR*.
- [63] Universal Robots, UR5e. 2021. <https://www.universal-robots.com/products/ur5-robot/>.
- [64] Jacob Varley, Chad DeChant, Adam Richardson, Joaquín Ruales, and Peter Allen. 2017. Shape completion enabled robotic grasping. In *2017 IEEE/RSJ International Conference on Intelligent Robots and Systems (IROS)* (Vancouver, BC, Canada). IEEE Press, 2442–2447. doi:10.1109/IROS.2017.8206060
- [65] Andreas Velten, Di Wu, Adrian Jarabo, Belén Masia, Christopher Barsi, Chinmay Joshi, Everett Lawson, Mouni Bawendi, Diego Gutierrez, and Ramesh Raskar. 2013. Femto-photography: capturing and visualizing the propagation of light. *ACM Transactions on Graphics (ToG)* 32, 4 (2013), 1–8.
- [66] Delio Vicini, Sébastien Speierer, and Wenzel Jakob. 2022. Differentiable signed distance function rendering. *ACM Transactions on Graphics (TOG)* 41, 4 (2022), 1–18.
- [67] Ignacio Vizzo, Benedikt Mersch, Rodrigo Marcuzzi, Louis Wiesmann, Jens Behley, and Cyrill Stachniss. 2022. Make it dense: Self-supervised geometric scan completion of sparse 3d lidar scans in large outdoor environments. *IEEE Robotics and Automation Letters* 7, 3 (2022), 8534–8541.
- [68] Mou Wang, Shunjun Wei, Jiadian Liang, Xiangfeng Zeng, Chen Wang, Jun Shi, and Xiaoling Zhang. 2021. RMIST-Net: Joint range migration and sparse reconstruction network for 3-D mmW imaging. *IEEE Transactions on Geoscience and Remote Sensing* 60 (2021), 1–17.
- [69] Peng-Shuai Wang, Yang Liu, and Xin Tong. 2022. Dual Octree Graph Networks for Learning Adaptive Volumetric Shape Representations. *ACM Transactions on Graphics (SIGGRAPH)* 41, 4 (2022).
- [70] Qingtao Wang, Tao Wang, Zhaohui Bu, Mengting Cui, Haipo Cui, and Li Ding. 2024. Segmentation-aided Upsampling for High-Resolution Reconstruction of 3D MMW Images. *IEEE Sensors Journal* (2024).
- [71] Yiduo Wang, Nils Funk, Milad Ramezani, Sotiris Papatheodorou, Marija Popović, Marco Camurri, Stefan Leutenegger, and Maurice Fallon. 2021. Elastic and efficient LiDAR reconstruction for large-scale exploration tasks. In *2021 IEEE International Conference on Robotics and Automation (ICRA)*. IEEE, 5035–5041.
- [72] Carl J Weisman. 2002. *The essential guide to RF and wireless*. Pearson Education.
- [73] Haozhe Xie, Hongxun Yao, Xiaoshuai Sun, Shangchen Zhou, and Shengping Zhang. 2019. Pix2vox: Context-aware 3d reconstruction from single and multi-view images. In *Proceedings of the IEEE/CVF international conference on computer vision*. 2690–2698.
- [74] Jiahong Xie, Hao Kong, Jiadi Yu, Yingying Chen, Linghe Kong, Yanmin Zhu, and Feilong Tang. 2023. mm3DFace: Nonintrusive 3D facial reconstruction leveraging mmWave signals. In *Proceedings of the 21st Annual International Conference on Mobile Systems, Applications and Services*. 462–474.
- [75] Hongfei Xue, Qiming Cao, Yan Ju, Haochen Hu, Haoyu Wang, Aidong Zhang, and Lu Su. 2022. M4esh: mmwave-based 3d human mesh construction for multiple subjects. In *Proceedings of the 20th ACM Conference on Embedded Networked Sensor Systems*. 391–406.
- [76] Hongfei Xue, Qiming Cao, Chenglin Miao, Yan Ju, Haochen Hu, Aidong Zhang, and Lu Su. 2023. Towards generalized mmwave-based human pose estimation through signal augmentation. In *Proceedings of the 29th Annual International Conference on Mobile Computing and Networking*. 1–15.
- [77] Hongfei Xue, Yan Ju, Chenglin Miao, Yijiang Wang, Shiyang Wang, Aidong Zhang, and Lu Su. 2021. mmMesh: Towards 3D real-time dynamic human mesh construction using millimeter-wave. In *Proceedings of the 19th Annual International Conference on Mobile Systems, Applications, and Services*. 269–282.
- [78] Jiaru Yang, Songpengcheng Xia, Yifan Song, Qi Wu, and Ling Pei. 2024. mmBaT: A Multi-Task Framework for Mmwave-Based Human Body Reconstruction and Translation Prediction. In *ICASSP 2024-2024 IEEE International Conference on Acoustics, Speech and Signal Processing (ICASSP)*. IEEE, 8446–8450.
- [79] Muhammet Emin Yanik, Dan Wang, and Murat Torlak. 2020. Development and demonstration of MIMO-SAR mmWave imaging testbeds. *IEEE Access* 8 (2020), 126019–126038.
- [80] Qian-Yi Zhou, Jaesik Park, and Vladlen Koltun. 2018. Open3D: A Modern Library for 3D Data Processing. *arXiv:1801.09847* (2018).
- [81] Yanzi Zhu, Yuanshuo Yao, Ben Y. Zhao, and Haitao Zheng. 2017. Object Recognition and Navigation using a Single Networking Device. In *Proceedings of the 15th Annual International Conference on Mobile Systems, Applications, and Services* (Niagara Falls, New York, USA) (*MobiSys '17*). Association for Computing Machinery, New York, NY, USA, 265–277. doi:10.1145/3081333.3081339